Detecting and characterizing pulsar haloes with the Cherenkov Telescope Array

Christopher Eckner, Veronika Vodeb, Pierrick Martin, Gabrijela Zaharijas, Francesca Calore

Monthly Notices of the ROYAL ASTRONOMICAL SOCIETY

MNRAS **521,** 3793–3809 (2023)
Advance Access publication 2023 March 9

https://doi.org/10.1093/mnras/stad715

Detecting and characterizing pulsar haloes with the Cherenkov telescope array

Christopher Eckner [1,2]★ Veronika Vodeb,[3] Pierrick Martin,[4] Gabrijela Zaharijas[3] and Francesca Calore[1]

[1] *LAPTh, CNRS, USMB, F-74940 Annecy, France*
[2] *LAPP, CNRS, USMB, F-74940 Annecy, France*
[3] *University of Nova Gorica, Center for Astrophysics and Cosmology, SI-5000 Nova Gorica, Slovenia*
[4] *IRAP, Université de Toulouse, CNRS, CNES, F-31028 Toulouse, France*

Accepted 2023 March 5. Received 2023 February 15; in original form 2022 December 21

ABSTRACT

The recently identified source class of pulsar haloes may be numerous and bright enough in the TeV energy range to constitute a large fraction of the sources that will be observed with the Cherenkov Telescope Array (CTA). In this work, we quantify the prospects for detecting and characterizing pulsar haloes in observations of the projected Galactic Plane Survey (GPS), using a simple phenomenological diffusion model for individual pulsar haloes and their population in the Milky Way. Our ability to uncover pulsar haloes and constrain their main physical parameters in the CTA GPS is assessed in the framework of a full spatial-spectral likelihood analysis of simulated survey observations, using the most recent estimates for the instrument response function and prototypes for the science tools. For a model setup representative of the halo around Geminga, we find that about three hundred objects could give rise to detectable emission in the GPS survey. Yet, only a third of them could be identified through their energy-dependent morphology, and only one-tenth of them would allow the derivation of strong constraints on key physical parameters like the magnitude or extent of suppressed diffusion around the pulsar. We also provide a list of known pulsars that could be hosting a detectable (Geminga-like) halo in the GPS and assess the robustness of our findings against several systematic uncertainties.

Key words: methods: data analysis – pulsars: general – Galaxy: disc – gamma-rays: galaxies.

1 INTRODUCTION

Over the past decade, pulsars have emerged as a significant class of objects in high-energy astrophysics, both as prominent sources in the gamma-ray sky over a broad spectral range, and as possible major contributors to the local flux of cosmic-ray leptons (Evoli et al. 2021).

In the GeV range, the *Fermi*-LAT has now detected more than 270 pulsars (Fermi-LAT collaboration 2022), which is a significant jump from the handful of objects known in the pre-Fermi era (Thompson 2008). Emission in this domain is produced by particle acceleration in the magnetosphere and/or in the striped pulsar wind beyond the light cylinder (Pétri 2016, 2018).

In the TeV range, three dozens sources were detected (Scott Wakely and Deirdre Horan 2022) that are established or candidate pulsar wind nebulae (PWNe), ∼1–10 pc-sized bubbles of hot magnetized plasma expanding beyond the pulsar wind termination shock and filled with non-thermal particles accelerated at the shock and/or in the immediate downstream turbulence (Amato 2020). Ground-based imaging Cherenkov telescopes (IACTs) like H.E.S.S., with their exquisite angular resolution, have played an instrumental role in the detection and study of PWNe (Abdalla et al. 2018a, b).

The chain of transport processes shaping the evolving morphology of PWNe is yet to be fully elucidated. Detailed studies of intermediate-age objects reveal intricate emission patterns, most likely influenced by the pulsar's natal kick and the dynamics of the parent supernova remnant (Abdalla et al. 2019; Principe et al. 2020), limiting our ability to predict the fate of non-thermal particles and the conditions of their release into the interstellar medium (ISM). At late stages, however, when the pulsar has left its parent remnant and the nebula develops a subparsec bow-shock morphology (Gaensler & Slane 2006; Bykov et al. 2017), particle escape may be more easily approached because the confinement volume is much smaller (although the physics driving it may still be rich and subtle, with energy- and charge-dependent effects; see Bucciantini, Olmi & Del Zanna 2020).

Observations with the High-Altitude Water Cherenkov observatory (HAWC) revealed extended gamma-ray emission from regions at least ∼20–30 pc in size around two middle-aged pulsars, PSR J0633+1746 and PSR B0656+14, respectively the Geminga pulsar and the pulsar in the Monogem ring (Abeysekara et al. 2017). This new source class seemingly consists of pulsar-powered emission from regions outside that dynamically dominated by the pulsar wind nebula and was originally dubbed TeV haloes (Linden et al. 2017). These objects provide an opportunity to study the feedback from and escape of particles accelerated in pulsars and their nebulae. Interestingly, the Geminga and Monogem haloes can be well described with a phenomenological diffusion model, provided the value of the

★ E-mail: eckner@lapth.cnrs.fr

diffusion coefficient in the vicinity of the pulsars is much lower than the average in the Galactic medium, by two to three orders of magnitude. This implies increased level of magnetic turbulence in extended regions around pulsars, and several scenarios have been put forward to account for it: standard magnetohydrodynamical turbulence with small coherence length, possibly in the wake of the expanding forward shock parent remnant (López-Coto & Giacinti 2018; Fang, Bi & Yin 2019), or self-confinement by pairs streaming from the pulsars (Evoli, Linden & Morlino 2018; Mukhopadhyay & Linden 2021).

Geminga and Monogem, being among the closest middle-aged pulsars, may just be the tip of the iceberg. Since the original discovery, a number of pulsar halo candidates were proposed based on HAWC (Linden et al. 2017; Albert et al. 2020), H.E.S.S. (Di Mauro, Manconi & Donato 2020), and more recently LHAASO observations (Aharonian et al. 2021). The phenomenon can be expected to cover a broad-band spectrum and can therefore be searched for also in *Fermi*-LAT data, although recent attempts to detect GeV counterparts to the Geminga and Monogem haloes are so far conflicting (Di Mauro, Manconi & Donato 2019; Xi et al. 2019). Yet, the exact physical grounds that lead to the development of pair haloes around (some) pulsars have yet to be exposed and, as a consequence, the commonness of pulsar haloes in the Galaxy is still largely unknown. Meanwhile, phenomenological models based on the assumption of suppressed diffusive transport within some distance of the pulsar provide a fairly good description of existing observations.

The detection and identification of a population of pulsar haloes, including measurements of their energy-dependent morphologies over a wide spectral range, is needed for a comprehensive modelling of non-thermal particle transport in the vicinity of pulsars and the connection of high-energy electron populations near their accelerators to those present in the Galactic medium (López-Coto et al. 2022). Continued observations with HAWC and LHAASO, and also with H.E.S.S. pending adaptation of data analysis to very extended sources (Abdalla et al. 2021), will no doubt be instrumental. In a few years from now, this effort will be contributed to by the Cherenkov Telescope Array (CTA), which holds special promise owing to its excellent angular resolution, broad energy coverage, and wider field of view when compared with current IACTs (Cherenkov Telescope Array Consortium 2019).

As part of an ensemble of Key Science Projects (Cherenkov Telescope Array Consortium 2019), an extensive survey of the full Galactic Plane will be performed with CTA, using both the Southern and Northern CTA observatories, resulting in unprecedented exposure, both in depth and footprint (the so-called Galactic plane survey, GPS). This effort will be accompanied by the production of catalogues (Remy et al. 2022) that will seed deeper investigations and provide opportunities for serendipitous discoveries, including TeV haloes.

In this work, we aim to assess the potential for the upcoming CTA experiment to constrain the current phenomenological halo models, based on the GPS observations. We determine the sensitivity of the survey to the emission spectrum and morphology predicted for individual haloes with different model setups. This is achieved in the framework of a full spatial-spectral likelihood analysis, using the most recent estimates for the instrument response function and prototypes for the science tools, and including an investigation of the effect of interstellar emission and data analysis systematics. We then frame the results in the context of a population synthesis, to estimate the fraction of the population that could be within the reach of CTA, and we provide a list of promising targets among known pulsars.

This paper is organized as follows: in Section 2, we present the different components that compose our model for the gamma-ray sky at TeV energies; in Section 3, we describe the procedure adopted to simulate the survey's observations, as well as the analysis framework; in Section 4, we illustrate the results of the CTA sensitivity to pulsar haloes, under different analysis' assumptions; we discuss the physics prospects and implications for the study of the pulsar haloes Galactic population in Section 5; finally, we draw our conclusions in Section 6.

2 SKY MODEL

In this section, we introduce the astrophysical emission components considered in our simulations and analyses of CTA observations. We first describe the phenomenological halo model and in particular the single representative model setup that is later used in our assessment for detectability of individual haloes. We then describe how such a model was used in another work by one of the authors to produce a synthetic halo population for the whole Galaxy, which we will use to infer the fraction of the sources that could be within reach of CTA in the context of GPS observations. At last, we present different models for the astrophysical background components considered in this work, namely the interstellar emission from the large-scale population of cosmic rays (CRs) of the Galaxy.

2.1 Individual halo model

The individual halo model and the reference parameter setups used in this work were introduced in Martin, Marcowith & Tibaldo (2022a) and derived mostly from the formalism presented in Tang & Piran (2019). We refer the reader to these publications for details and just summarize here the salient features of the model.

A few tens of kyr after pulsar birth, when, as a result of its natal kick, the pulsar exits its parent remnant or the original pulsar wind nebula, electron–positron pairs accelerated in the now bow shock pulsar wind nebula are released into the surrounding medium. This happens on short time-scales, mainly due to the small subparsec size of the object. Particles then diffuse away isotropically in a medium characterized by a two-zone concentric structure for diffusion properties. An outer region is representative of the large-scale average ISM in the Galactic plane, while the inner region with a radial extent of a few tens of pc has diffusion suppressed by factors of a few tens to a few hundreds as a result of an unspecified physical mechanism (for instance pre-existing fluid turbulence with small coherence length or self-confinement of the streaming pairs). Along their propagation, particles lose energy and radiate via the synchrotron and inverse-Compton scattering processes, in magnetic and radiation fields assumed to be typical of the ISM.

In the absence of a consistent physical description for the very origin of particle confinement around (some) pulsars, the conditions for suppressed diffusion are assumed to be static and the suppressed diffusion coefficient follows a power-law rigidity dependence with index 1/3, applicable for scattering in magnetic turbulence with a Kolmogorov spectrum. Following Martin et al. (2022a, b), we considered different possible scenarios for the diffusive haloes: three different radial extensions of the suppressed diffusion zone (30, 50, or 80 pc), and two levels of diffusion suppression with respect to large-scale interstellar conditions (by a factor 500, as required by observations of J0633+1746, or by a factor 50, in agreement with observations of B0656+14 within uncertainties as shown in Martin et al. (2022a); in practice this translates into diffusion coefficients of 4×10^{27} and 4×10^{28} cm^2 s^{-1} at 100 TeV , respectively).

We consider, as baseline model, a halo with the following properties:

(i) A pulsar with a current age of 200 kyr, spin-down power of 10^{35} erg s^{-1} , and spin-down evolution with a braking index of 3;
(ii) Particle injection is assumed to start 60 kyr after pulsar birth and to last until the current pulsar age with a constant injection efficiency initially set at 100 per cent;
(iii) Injected particles have a constant broken power-law spectrum from 1 GeV up to a cutoff at 1 PeV , with indices 1.5 and 2.4 below and above a break at 100 GeV , respectively;
(iv) A suppressed diffusion region size of 50 pc and a level of diffusion suppression in this region by a factor 500;
(v) The interstellar magnetic and radiation fields are those corresponding to a position at (R, z) = (4500 pc, 0 pc) in the Galactic population synthesis of Martin et al. (2022b);
(vi) The effects of proper motion on the halo morphology are neglected, which is justified by the fact that very-high-energy signatures of haloes are little sensitive to it (Zhang et al. 2020).

The 60 kyr start time for particle injection is the typical time at which a pulsar enters the bow-shock phase, during which accelerated particles are expected to escape the nebula quite rapidly. It corresponds to the time when the pulsar exits its parent remnant, or the original nebula at its centre, owing to its natal kick (see the discussion in Martin et al. 2022a). The 1 PeV cutoff energy exceeds by a factor $\sim$2 the highest particle energy that can be reached from the maximum potential drop under the assumption of ideal magnetohydrodynamics (de Oña Wilhelmi et al. 2022). In a population study perspective, the exact maximum energy in the particle spectrum has a limited influence on the prospects as the CTA sensitivity to haloes is mostly found at gamma-ray energies below a few tens of TeV (see Section 4), in a range where the signal is mostly contributed to by $\lesssim$100 TeV particles inverse-Compton scattering infrared photon fields (see also the discussion in section 2.1 of Martin et al. 2022a).

Variants of the above model setup were computed for alternative suppressed diffusion region sizes (30 or 80 instead of 50 pc) and level of diffusion suppression (50 instead of 500). 3D model cubes for these individual halo model setups were computed over a range of distances from 1 to 15 kpc, at the reference coordinates $(l, b) = (-10^{\circ}, 0^{\circ})$ used in our assessment of the prospects for detection and study (see Section 3.2). We note that putting this test halo model at various distances from 1 to 15 kpc for the reference position causes an inconsistency because the interstellar magnetic and radiation fields used by default are not appropriate to all locations considered. Yet, we decided not to change distance and environmental conditions at the same time to avoid mixing too many different effects in the detectability trends.

When deriving prospects for detectability in the following, a given halo model setup will be renormalized to the minimum value required to achieve a given scientific goal (for instance simple detection with TS = 25, or detection as an energy-dependent extended source). This is done via the injection luminosity $L_{\rm inj}$ parameter, which is the product of injection efficiency and present-day spin-down power.

2.2 Halo populations model

The individual halo model setups described above were used to assess the conditions under which a typical halo can be observed in the CTA GPS. This means, for instance, evaluating the particle injection power required for a halo to be detected as an extended source with an energy-dependent morphology. Such constraints determined on representative halo models are then compared to the properties of a Galactic synthetic population to infer the number of objects that could be accessible to the survey. For that purpose, we used a halo population synthesis that was introduced in Martin et al. (2022b) and we just summarize here its main features.

The full population model starts with the generation of a synthetic population of young pulsars, with random selection of positions, powers, natal kick velocities, and ages. Each pulsar initially feeds a PWN until the time when it exits its nebula, which marks the beginning of the halo phase. Haloes are modelled as described in the previous section and all objects in a given population share the same properties for the suppressed diffusion region. Conversely, the properties of injected particles were randomly selected from statistical distributions of power-law indices above the break energy, cutoff energies, and injection efficiencies. The parameters of the entire population of sources, haloes, and PWNe (and also SNRs), were calibrated so that the flux distribution of mock objects in the TeV range match that of known sources. A typical realization of the population includes about 2600 objects, with ages from 20 to 400 kyr, and 1–10 TeV luminosities in 10^{30}–10^{34} erg s^{-1} .

We emphasize here a caveat in the approach defined above: when assessing the detectable fraction of the population in Section 5.2, we will compare haloes from a synthetic population comprising a large variety of conditions (pulsar age, magnetic and radiation field intensities, particle injection start time and spectrum,...) with detectability criteria that are strictly valid for only one set of halo model parameters. Yet, assessing the detectability for a large number of halo parameters combinations would have been prohibitive computationally speaking, hence our choice of the above approach. For that reason, the prospects at the population level, introduced in Section 5.2, should be taken as approximations.

2.3 Large-scale diffuse backgrounds

In addition to the emission from pulsar haloes, and the instrumental background that will be introduced in the next section, we included in our analyses a model for large-scale interstellar emission (IE) from interactions of the Galactic population of CRs with the ISM. Such a component can have important effects on the individual detectability of extended sources like haloes.

The IE runs predominantly along the Galactic plane and has been exquisitely mapped with the *Fermi*-LAT at GeV energies, where it is the brightest emission component in the sky (see Ackermann et al. 2012 for a review). In the TeV range, however, the properties of this source are less solidly established, in part because of difficulties to detect emission components extending over angular scales larger than the field of view with IACTs. As concerns previous IE studies with IACTs, the H.E.S.S. collaboration published an assessment of diffuse emission along the Galactic plane (Abramowski et al. 2014). Owing to data analysis limitations, the measurement is a mix of unresolved emission from populations of sources and truly interstellar radiation, with limited recovery of its spatial structure on small scales. Although the authors estimate that gamma-ray emission from π^0-decay accounts for a significant fraction of the signal, the cumulative nature of the measurement and the lack of detailed morphological constraints prevents its use in our work. There has been, however, recent progress in this domain thanks to the advent of ever-sensitive water-Cherenkov detectors like MILAGRO, HAWC, or LHAASO, owing to their very large effective area and instantaneous field of view and high duty cycles.

In order to model this component we take advantage of a recent study (De la Torre Luque et al. 2022) based on available GeV to PeV gamma-ray data (from *Fermi*-LAT, Tibet ASγ, LHAASO, and

ARGO-YBJ), together with local charged CR measurements (from AMS-02, DAMPE, CALET, ATIC-2, CREAM-III, and NUCLEON). Modelling the IE is achieved within two physical frameworks: in the so-called 'Base' models the diffusion coefficient is assumed to be constant throughout the Galaxy, while it is allowed to vary radially in the 'γ-optimized' models. Both sets of models are further divided in 'Min' and 'Max' setups in order to reflect uncertainties in the CR proton and Helium source spectra, see De la Torre Luque et al. (2022) for more details. We chose the 'Base Max' setup as our benchmark model, but explored in Section 4.2.3 the impact on the derived sensitivities to haloes of using 'γ-optimized Min' model instead.

For consistency, we also consider a model adopted in a reference prospect study of the CTA GPS (the so-called 'GPS IEM' in Dundovic et al. 2021). This model is tuned to direct CR measurements near the Earth, but agnostic to current gamma-ray measurements that indicate higher and harder CR spectra in central regions of the Galaxy. The 'GPS IEM' model therefore represents a minimal contribution expected from IE at TeV energies.

3 DATA SIMULATIONS AND ANALYSIS

3.1 Simulation of survey observations

The CTA GPS will provide a view of the Galactic Plane at TeV energies with unprecedented depth, angular resolution, and spectral coverage. The observational campaign will consist of a short-term programme, with 480 h of observing time allocated over the first two years, and a long-term programme, with 1140 h of observing time allocated over the following eight years (Cherenkov Telescope Array Consortium 2019). Regarding the practical implementation of the survey in our simulations, we followed the same approach as in Remy et al. (2022). Observations are distributed along the plane following a double-row pointing pattern and data are taken by both the North and South arrays, according to a preliminary schedule that reduces contamination by Moon light and minimizes zenith angle in each observation, so as to optimize the performances of the instrument (Remy et al. 2022).

Due to the different configurations of the North and South arrays, and because of the particular importance of specific regions in our Galaxy, the planned exposure in the GPS varies along the plane and has been divided into five segments: Inner Galaxy, Cygnus/Perseus, Anticentre, and two chunks for Vela/Carina (Cherenkov Telescope Array Consortium 2019). The anticipated exposure is illustrated in Fig. 1 for the Inner Galaxy within longitudes $-60^\circ < l < 60^\circ$ and latitudes $-3^\circ < b < 3^\circ$ (for full exposure see Appendix B). This region will be observed with the deepest exposure as it harbours the largest density of sources. Since this is also the region where the majority of young pulsars, hence pulsar haloes, are expected, we use as reference position for our study the coordinates $(l, b) = (-10^\circ, 0^\circ)$. On the other hand, this may appear as a conservative choice, since the Inner Galaxy is where IE is the most intense at this position.

We used the most recent instrument response functions (IRFs) for the observatory[1], labelled `prod5`, for the envisaged configurations of the North and South sites. The respective IRF data files are publicly available at Cherenkov Telescope Array Observatory and Cherenkov Telescope Array Consortium (2021). We used by default the 'alpha' configuration, which refers to the arrays that will be built in an initial

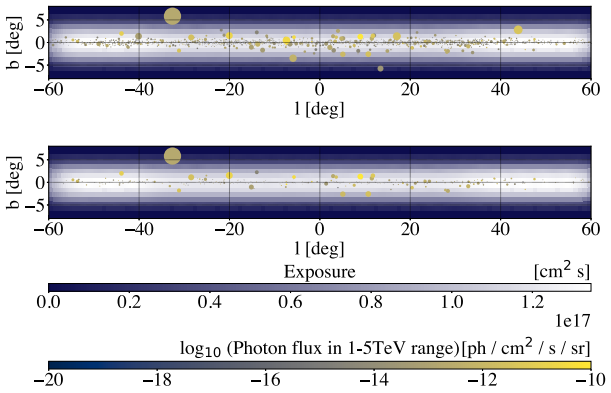

Figure 1. The 0.1–100 TeV exposure for the planned GPS observations overlaid with one realization of a synthetic pulsar halo population. Top: All simulated sources. Bottom: Only resolved sources (see Section 5.2).

phase of the project, with a realistic number of telescopes given the currently secured budget. The spatial distribution of telescopes in this configuration has been optimized for performance across a series of science goals.

In practice, we selected the set of IRFs corresponding to event reconstruction quality and background cuts optimized on the basis of Monte Carlo simulations of 50 h of observations, which is appropriate for studies of extended sources. By background, we refer here to air showers triggered by CR particles entering the atmosphere that can be misidentified as gamma rays in the event reconstruction process. These actually make up the largest fraction of the events detected by ground-based observatories, and this will remain true for the CTA. The misidentified CR component is modelled from extensive Monte-Carlo simulations of CR air showers, detection of the associated Cherenkov radiation, and subsequent event reconstruction. The corresponding rate and distribution of misidentified CR events is provided with the suite of IRFs for each given set of observing conditions (duration, zenith angle,...). There are however significant uncertainties or biases in this predicted component, in normalization, spectrum, and spatial distribution within the field of view, such that, in an actual data analysis, it is generally needed to fit in the data (simultaneously to the models for the emission of astrophysical sources). In the spatial-spectral likelihood analysis introduced below, the normalization of the CR background is therefore left free, which is a minimum assumption to cover the uncertainties in this component. Last, simulations and analyses were performed using the publicly available gamma-ray analysis software `ctools`[2]

3.2 Analysis framework

To evaluate our capability to detect and study pulsar haloes with CTA, we adopt the statistical inference framework of Acharyya et al. (2021) – there employed in the context of indirect searches for a continuum gamma-ray signal from dark matter pair-annihilation in the Galactic centre region with CTA – and adapt it to our needs.

Source characterization in simulated GPS observations is achieved by maximum-likelihood estimation of the parameters of an emission model for some region of interest. We perform a 3D likelihood analysis for binned data and Poisson statistics. Unless otherwise stated, the analysis is performed under the following conditions:

[1] see http://www.cta-observatory.org/science/cta-performance/ for more details

[2] http://cta.irap.omp.eu/ctools/

(i) Region of interest (ROI) centred on $(l, b) = (-10^\circ, 0^\circ)$, with $6^\circ \times 6^\circ$ size, aligned on Galactic coordinates, with $0.02^\circ \times 0.02^\circ$ pixel size.

(ii) Energy range from 0.1 to 100 TeV, binned logarithmically with 15 bins per decade.[3] Energy dispersion is not used.

Our model for the signal in the ROI is based on templates of the expected instrumental background $\{B_l\}_{l \in L}$ and astrophysical signal components $\{S_k\}_{k \in K}$ with L and K being index sets for each series of templates (for instance different background noise templates for the different pointings in a data set, and different emission components for the region of the Galactic plane under scrutiny). The Poisson likelihood function reads

$$\mathcal{L}(\boldsymbol{\mu}|\boldsymbol{n}) = \prod_{i,j} \frac{\mu_{ij}^{n_{ij}}}{(n_{ij})!} \mathrm{e}^{-\mu_{ij}}, \tag{1}$$

where $\boldsymbol{\mu}$ denotes the user-defined model cube describing the signal whereas $\boldsymbol{n}$ refers to the experimental data taken by CTA, here realized via simulated 'mock' observations. The index i labels the energy bins while the index j enumerates the spatial pixels of our templates. Our model is a linear combination of templates describing distinct contributions to the signal received by the instrument. In the most general form

$$\boldsymbol{\mu} = \sum_{k \in K} \boldsymbol{S}_k(\theta_k^S) + \sum_{l \in L} \boldsymbol{B}_l(\theta_l^B), \tag{2}$$

where the vector sets $\{\theta_k^S\}_{k \in K}$ and $\{\theta_l^B\}_{l \in L}$ are parameters affecting the spectral and angular dependence of the astrophysical signal and instrumental background noise templates, respectively. In practice, however, most of the cases we handle involve a global renormalization of predefined astrophysical signal and instrumental noise templates, possibly with an energy dependence in the case of the instrumental noise, such that the model prediction reads

$$\mu_{ij} = \sum_{k \in K} \theta_k^S S_{k,ij} + \sum_{l \in L} f_i^B(\theta_l^B) B_{l,ij}. \tag{3}$$

The presence of a spectral correction $f_i^B(\theta_l^B)$ in the case of instrumental background is warranted by our imperfect knowledge of the instrumental response in realistic conditions, and therefore the possibility of a cross-talk between components when testing a given extended astrophysical model.

Our ability to discriminate between alternative hypotheses regarding the composition of the measured signal within a particular ROI is assessed via the log-likelihood ratio test statistic (TS), which quantifies the significance of the improvement provided by a test hypothesis over a null hypothesis when compared to the data. In general, the TS reads

$$\mathrm{TS} = 2 \left(\ln \left[\frac{\mathcal{L}\left(\boldsymbol{\mu}(\{\hat{\theta}_k^{S_{\mathrm{test}}}\}, \{\hat{\theta}_l^B\})|\boldsymbol{n}\right)}{\mathcal{L}\left(\boldsymbol{\mu}(\{\hat{\theta}_k^{S_{\mathrm{null}}}\}, \{\hat{\theta}_l^B\})|\boldsymbol{n}\right)} \right] \right), \tag{4}$$

where hatted quantities refer to the best-fitting values for all model parameters (astrophysical signal and instrumental background noise) obtained after a maximum-likelihood fit to the mock data using equation (1). By profiling over the background parameters, we treat them as nuisance parameters. Examples of hypotheses that will be tested in the following include simple detection of a model component (the null hypothesis is a fit without that model component), detection of the pulsar halo signal beyond a certain physical radius (the null hypothesis is a fit with a model clipped to zero beyond that radius), or the detection of the halo energy-dependent morphology (the null hypothesis is a fit with an energy-independent model such as a 2D Gaussian).

3.3 Detectability estimates

In the simple case where the detection of astrophysical components is tested, equation (4) reduces to

$$\mathrm{TS}_{\mathrm{det}} = 2 \left(\ln \left[\frac{\mathcal{L}\left(\boldsymbol{\mu}(\{\hat{\theta}_k^S\}, \{\hat{\theta}_l^B\})|\boldsymbol{n}\right)}{\mathcal{L}\left(\boldsymbol{\mu}(\{\theta_k^S = 0\}, \{\hat{\theta}_l^B\})|\boldsymbol{n}\right)} \right] \right). \tag{5}$$

The significance of the detection is given by the value of the test statistic and depends on the number of signal components. It can be shown that, under a set of regularity conditions, statistical fluctuations in the absence of signal components in the data result in $\mathrm{TS}_{\mathrm{det}}$ being distributed according to a non-central χ^2-distribution with K degrees of freedom (Cowan et al. 2011). In what follows, we usually consider the case where we only have a single signal template. In this particular case, we find that the distribution $p(\mathrm{TS}_{\mathrm{det}})$ reads:

$$p(\mathrm{TS}_{\mathrm{det}}) = \frac{1}{2} \left(\delta(\mathrm{TS}_{\mathrm{det}}) + \frac{1}{\sqrt{2\pi\,\mathrm{TS}_{\mathrm{det}}}} \mathrm{e}^{-\frac{\mathrm{TS}_{\mathrm{det}}}{2}} \right), \tag{6}$$

where δ is the Dirac δ-distribution. The entire probability distribution is sometimes called a half-χ^2-distribution with one degree of freedom. The test statistic value corresponding to a signal detection at the 5σ level is $\sim$25.

3.4 Sensitivity analysis

Spectral sensitivity: Differential spectral sensitivity was computed over the full energy range for 5 bins per decade, which implies casting the original binning of our model templates on a coarser grid (see Section 3.2). The sensitivity to a given source of interest in each independent energy bin is computed as the flux level yielding a detection with a TS = 25 and providing at least ten detected gamma-ray events in that bin alone.[4] Mock observations are simulated from an emission model containing the instrumental background noise and astrophysical signal components (the source of interest and possibly another component such as the IE model). For a given normalization of the component for the source of interest and in a given energy bin, a TS is computed from the likelihoods obtained in two fits: a fit for the test hypothesis in which the emission model consists in all components used in the data simulation, and a fit for the null hypothesis in which the component for the source of interest was removed. The normalization of the source of interest is iteratively adjusted and the observation simulation and data analysis sequence is repeated until the TS converges towards a value of 25 in that energy bin for that source of interest.

Model-independent angular sensitivity: Angular sensitivity was computed over three energy bands (0.1–1, 1–10, and 10–100 TeV), which implies reducing our original binning scheme to just three 2D maps. We used a similar approach as for the spectral sensitivity analysis and searched for the normalizations of a set of N concentric uniform-brightness annuli with mean radii $\{r_i\}$ and widths $\{\Delta r_i\}$,

[3] We use 15 logarithmically spaced energy bins to ensure that the IRFs are properly sampled. This finer binning is summed into larger energy bins before performing the analysis.

[4] We do not implement an additional constraint demanding a signal to background ratio of at least 1/20, as done to obtain the differential sensitivity curves shown in the CTAO performance page for `prod5` IRFs.

with $i = 1...N$, such that each annulus is individually detected with TS = 25 in a given energy range. We assumed a fixed power-law spectrum with photon index 2.0 for each annulus and typically used $\Delta r_i = 0.2^\circ$ and angular distances from the centre of the ROI $r_i = 0^\circ...3^\circ$. Mock observations are simulated from an emission model containing the instrumental background noise, an interstellar emission template, and one given annulus. For a given brightness of the annulus, a TS is computed in each energy range from the likelihoods obtained in two fits: a fit for the test hypothesis in which the emission model consists in all components used in the data simulation, all with free normalizations, and a fit for the null hypothesis in which only the instrumental background noise and interstellar emission templates are fitted. The brightness of the annulus is iteratively adjusted and the observation simulation and data analysis sequence is repeated until the TS converges towards a value of 25 for that annulus in that energy range. The process is performed for all annuli independently in all three energy ranges.

3.5 Angular decomposition of a pulsar halo signal

We perform an angular decomposition of individual pulsar haloes modelled as introduced in Section 2.1. We start from a given mock data set $\boldsymbol{n}$ derived from templates for the instrumental background, IE, and a pulsar halo for a particular choice of injection power, diffusion region size, and distance to the Sun, with all components included at their nominal values according to the utilized flux models, i.e. $\theta_k^S \equiv 1, \theta_l^B \equiv 1\ \forall k \in K, l \in L$. We conduct successive fits of a growing number of concentric annuli of fixed width Δr, obtained by truncating the original pulsar halo model. The successive fit rationale is as follows: starting with the central annulus – a disc of radius Δr – as the only pulsar halo component in the model $\boldsymbol{\mu}$, we evaluate equation (5), which either yields $\mathrm{TS_{det}} < 25$ or $\mathrm{TS_{det}} > 25$. In the $\mathrm{TS_{det}} < 25$ case, we increase the annulus width until we either get $\mathrm{TS_{det}} > 25$ and continue the iterative fit, or a maximum allowed width is reached and we stop the decomposition. In the $\mathrm{TS_{det}} > 25$ case, we continue by treating the previously considered annulus as an astrophysical components and adding the next annulus to the model. We evaluate again equation (5) with the model now containing the additional second annulus and determine whether this new component is significantly detected, i.e. the model including the two annuli is statistically favoured over that containing only the first annulus. In case of a positive result, i.e. $\mathrm{TS_{det}} > 25$ is obtained for the additional annulus, we iterate this procedure until adding another annulus to the fit does not result in any significant improvement. Eventually, the best-fitting parameters and errors for all significant annuli in the last iteration step are taken as the recovered angular decomposition of the input signal.

3.6 Treatment of systematics

The Poisson-likelihood function in equation (1) incorporates knowledge about the probabilistic nature of the process to detect gamma rays and makes it possible to deal with the statistical uncertainty of a measurement arising due to its Poisson nature. However, CTA is going to observe the Galactic plane for an extensive period of time and large amounts of data will be accumulated, such that we will transition from a statistics-limited regime to a systematics-dominated one in a certain energy range. This means that, after this transition, taking additional data does not improve the sensitivity of the instrument anymore since systematic effects and uncertainties become relevant and may bias the search for a certain signal. To characterize the expected impact of systematic uncertainties, we introduce an effective Poisson-likelihood function (see Silverwood et al. (2015) for a more detailed explanation)

$$\mathcal{L}(\boldsymbol{\mu}, \boldsymbol{\alpha} | \boldsymbol{n}) = \prod_{i,j} \frac{(\mu_{ij}\alpha_{ij})^{n_{ij}}}{\sqrt{2\pi}\sigma_\alpha n_{ij}!} \mathrm{e}^{-\mu_{ij}\alpha_{ij}} \mathrm{e}^{\frac{(1-\alpha_{ij})^2}{2\sigma_\alpha^2}}, \quad (7)$$

which modifies the standard likelihood function through the addition of nuisance parameters $\boldsymbol{\alpha}$ centred around one with variance σ_α^2 per pixel and energy bin of the binned model. These nuisance parameters can be seen as Gaussian noise that affects each pixel independently of the others leading to up- or downward fluctuations. However, this effective treatment of systematic uncertainty can only cover such sources of uncertainty that enter linearly in the calculation of the number of expected gamma rays, for instance, the effective area of CTA. Incorporating non-linear effects is much more involved. It requires the use of Monte Carlo simulations to estimate the likelihood landscape of such contributions, which goes beyond the scope of this work and analyses based on simulated mock data in general.

To derive detection sensitivities in the framework of equation (7), we add the parameters $\boldsymbol{\alpha}$ to the set of background parameters that are profiled over in equation (5). We remark that this implementation of systematic errors introduces a certain dependence on the binning of the utilized templates in terms of a characteristic length scale equal to the spatial bin size. Since this prescription assumes all pixels to be affected independently of each other by the systematic effects, it is a statement about the statistical independence of the pixels, which is a priori not guaranteed. A more detailed discussion of this limitation can be found in Refs. Bartels, Gaggero & Weniger (2017); Acharyya et al. (2021). We discuss the impact of systematic uncertainties for the detection and characterization of pulsar haloes in Section 4.2.3.

4 CTA SENSITIVITY TO PULSAR HALOES

4.1 Model-independent sensitivity to extended sources

We start with a general study of the sensitivity of the GPS to extended (Gaussian) sources, since the physical processes governing the development of pulsar haloes are still poorly known and because such a study could be valuable when assessing the detection prospects for other source classes, for instance PWNe, star-forming regions, or dark matter clumps.

In Fig. 2 (left-hand panel), we show the spectral sensitivity to 2D Gaussian intensity distributions with various energy-independent extensions. The sensitivity degrades with an increasing source size by about an order of magnitude over most of the energy range when going from the point-like case up to $\sigma = 1.0^\circ$. The spectral sensitivity curves presented above do not provide any information about the angular size over which a given extended source is significantly detected. We therefore display in Fig. 3 (left-hand panel) curves showing angular sensitivity to uniform ring emission in three different energy ranges: 0.1–1 , 1–10 , and 10–100 TeV . For details on how such sensitivities are calculated see Section 3.3.

4.2 Sensitivity to a physical model of pulsar haloes

In this section we turn instead to simulating pulsar halo emission following the physical model proposed in Martin et al. (2022a). In this case, the gamma-ray extension of the halo is set by the assumed setup of the model and is in the general case energy dependent, in contrast to our Gaussian scenario above.

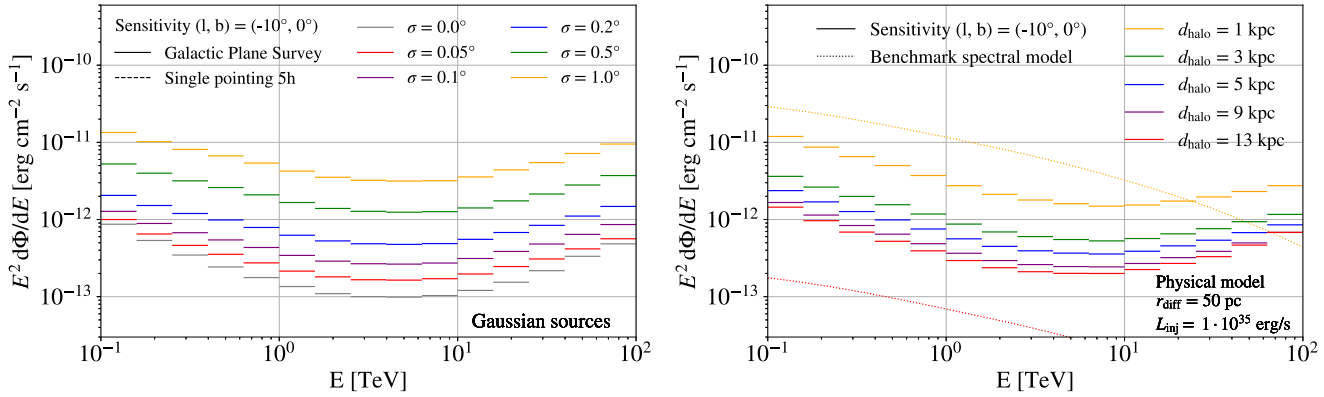

Figure 2. Differential spectral sensitivity to extended sources for the Galactic Plane survey observations, focusing on a 6 degree region centred at $(l,\ b) = (-10°, 0°)$. Left-hand panel: Differential sensitivity to extended Gaussian sources with extensions ranging between 0.0° and 1.0°. The full lines show the sensitivity for the Galactic Plane survey, while the dashed lines mark the differential sensitivity to an extended Gaussian source assuming a 5h single pointing observation with the Southern array and using `prod5` IRFs optimized for 20° zenith angle. The same colours correspond to the same source extensions. Right-hand panel: Differential sensitivity to our benchmark pulsar halo model for the Galactic Plane survey observations, positioned at different distances from the observer. The dotted lines show the benchmark spectral model for pulsar haloes. The same colours correspond to the same source distance.

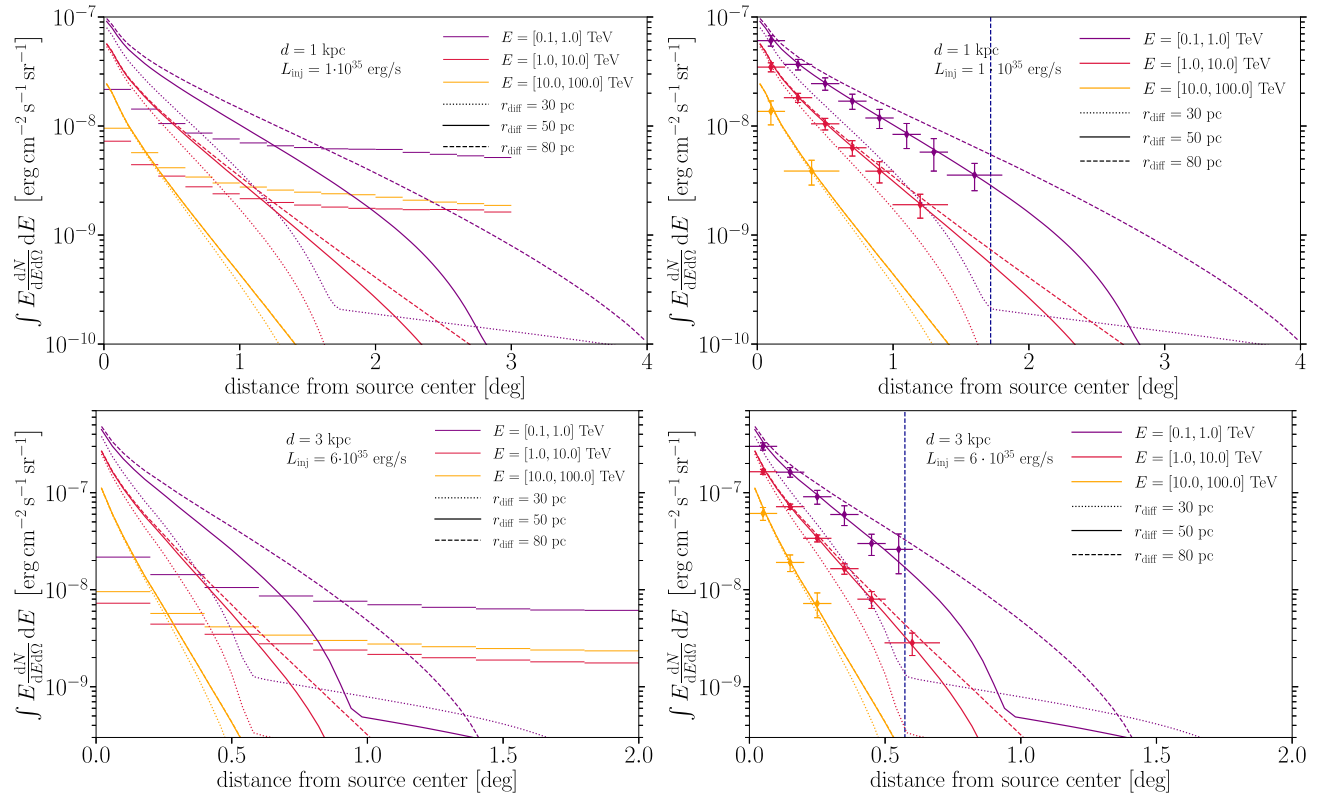

Figure 3. Model-independent (left-hand panel) and model-dependent (right-hand panel) angular sensitivity in the three energy bands (0.1–1, 1–10, and 10–100 TeV), plotted together with the predicted intensity of pulsar halo models with a diffusion region size of 30 pc (dotted lines), 50 pc (full lines), and 80 pc (dashed lines) located at $(\ell,\ b) = (-10°, 0°)$ at 1 kpc distance from the observer and an injection power of $L_{\rm inj} = 1 \times 10^{35}$ erg s^{-1} (top) or at 3 kpc distance from the observer and an injection power of $L_{\rm inj} = 6 \times 10^{35}$ erg s^{-1} (bottom) studied under the conditions of CTA's Galactic plane survey. The injection power has been chosen so that the haloes are above the yellow line in Fig. 5 allowing for an angular decomposition out to at least 30 pc (denoted by a blue vertical line). Left-hand panel: Angular sensitivity to uniform brightness annuli with a fixed width of 0.2°. Right-hand panel: Prospects for an angular decomposition study of the benchmark pulsar halo with a diffusion zone size of 50 pc. The halo has been decomposed into annuli following the prescription in Section 3.4 with a minimal width of 0.2° for $d = 1$ kpc and 0.1° for $d = 3$ kpc as indicated by the horizontal error bars. The vertical error bars denote the statistical uncertainty of the reconstructed flux within the found annulus.

4.2.1 Spectral sensitivity

The spectral sensitivity, shown in the right-hand panel of Fig. 2 for a 50 pc suppressed diffusion region, degrades with an increased extension of the halo, resulting from a closer location, as also found for the general Gaussian source case (see Section 4.1). The sensitivities to physical halo models are roughly consistent with those of a Gaussian source (left-hand panel of Fig. 2) of the corresponding angular size (the containment radius of the halo emission, which is energy-dependent but typically of the order of the suppressed diffusion region extent, placed at the corresponding $d_{\rm halo}$ distance; as a reference, the angular radius of a 50 pc extent placed at a distance of 1 (5, 13) kpc, is 1.43°(0.29°, 0.11°)). The sensitivities to the physical halo model, however, tend to be flatter with increasing energy as a result of the source size shrinking with energy, owing to stronger energy losses with increasing particle energy, which counterbalances the otherwise degrading sensitivity of the instrument beyond about 10 TeV .

For increasing distances, the sensitivity initially improves roughly with the inverse of the distance, because the same halo signal is mixed with instrumental background over a smaller area, but that trend tends to flatten for distances $\gtrsim$ 4–5 kpc, when the typical angular size of the halo becomes comparable to or smaller than the angular resolution of the instrument. In the meantime, the flux from a halo decreases with the inverse of the distance squared.

Fig. 2 displays the flux levels of our reference individual halo model, for comparison to the computed spectral sensitivities. The reference halo model features a present-day injection luminosity of 10^{35} erg s^{-1} , or about five times the one involved in Geminga (Martin et al. 2022a). We did not investigate prospects for haloes closer than 1 kpc because their typical extent would exceed the latitude extent of the survey. Such objects would require additional, dedicated observations. Our results suggest that fine spectral studies from a few hundreds of GeV to a few tens of TeV would be possible for nearby haloes at distances 1–3 kpc and involving injection powers a few times above that inferred for Geminga, or about 10^{35} erg s^{-1} . We will see in Section 5.2 that two to three dozens of pulsars with properties possibly in that range are known. At larger distances, above 5 kpc, the power requirement for fine spectral studies increases to about 10^{36} erg s^{-1} or more, which certainly reduces the pool of possible targets since not many middle-aged pulsars have retained such a power.

4.2.2 Angular sensitivity

In this section, we assess the capability of the CTA to resolve the angular profile of pulsar haloes. This is done in two steps: we first compare the intensity distribution of various halo models to estimated model-independent angular sensitivity curves in three energy bands, computed following the methodology exposed in Section 3.4; we then perform an angular decomposition from mock observations of these given halo models, to confirm the prospects suggested in the first step.

The left-hand panels in Fig. 3 show angular sensitivity curves obtained for a set of concentric uniform-brightness annuli. These are compared to our reference halo model at 1 and 3 kpc, for different suppressed diffusion region sizes, and scaled for injection powers of 10^{35} and 6×10^{35} erg s^{-1} , respectively. These normalizations were chosen so that a meaningful angular decomposition over a sufficient number of angular bins could be achieved. In the 1 kpc case, the halo profile for a 50 pc suppressed diffusion region lies above sensitivity out to about 1.5 deg from the centre in the two lower energy ranges, and only out to 0.5 deg in the higher energy range. This corresponds to lengths of 26 and 9 pc at a distance of 1 kpc, respectively. These statements are dependent on the extent of the suppressed diffusion region, especially at the lowest energies. Overall, the CTA GPS should allow us to probe the 0.1–10 TeV intensity distribution of a pulsar halo with power 10^{35} erg s^{-1} and at distance 1 kpc over an extent comparable to that reached by HAWC for Geminga (Abeysekara et al. 2017). This is confirmed by the actual angular decomposition performed from mock observations based on the same halo model (see the top right-hand panel in Fig. 3). In the 3 kpc case, qualitatively similar results are obtained, at the expense of a six times higher injection power.

4.2.3 Robustness of results

In this section we explore how dependent our results are on (i) the assumption we make on the IE model and (ii) instrumental systematic uncertainties. We address this issue by quantifying how our benchmark sensitivity to haloes changes when relaxing particular assumptions. Specifically, we focus on two cases: a significantly extended halo positioned at 1 kpc (Fig. 4, left-hand panel), and a point-like halo positioned at 13 kpc distance (Fig. 4, right-hand panel).

Impact of the IE model: In Fig. 4 we explore the impact of three different assumptions: no IE case (where only the CR background is present), γ-optimized Min model from De la Torre Luque et al. (2022) and the IE model that is used in GPS publication (see Remy et al. 2022). We observe that, as expected, the impact of IE is larger in the case of an extended source (left-hand panel) but it is limited to less than 20 per cent impact. Note that here we assume that we know the true IE model. In a more realistic case where data are produced with one model (say Base Max), and modelled with another (say γ-optimized Min), the sensitivities can degrade significantly. In Appendix C, we explore the worsening of sensitivities from using different combinations of IE models for data production and modelling. We find that the sensitivities degrade by a factor of up to 4.

Systematic uncertainty: The template likelihood analysis adopted here critically depends on having appropriate models for the emission components. However, many instrumental effects, especially those that affect the observations within the field of view on smaller scales are notoriously hard to model, but could have significant impact on the analysis (see discussion in Acharyya et al. 2021). While the exact level or scale of such potential effects are unknown before the construction of the instruments, we follow Acharyya et al. (2021) in choosing the scale of 0.1° (close to the PSF size) and plot its impact for the magnitude of 1 per cent (which is the target goal of the CTA) and 3 per cent. We note that, as expected the impact of these uncertainties is the highest at low energies (since higher energies are statistics dominated) and are limited to $\leq$ 10 per cent at around 1 TeV where we have the best sensitivity to our sources.

5 PHYSICS PROSPECTS

5.1 Insights for individual haloes

When using the halo around Geminga as a canonical instance of the phenomenon (especially in terms of diffusion suppression level), most of the signal above a few TeV is contained within 20–30 pc of the pulsar and is thus little sensitive to the full extent of the

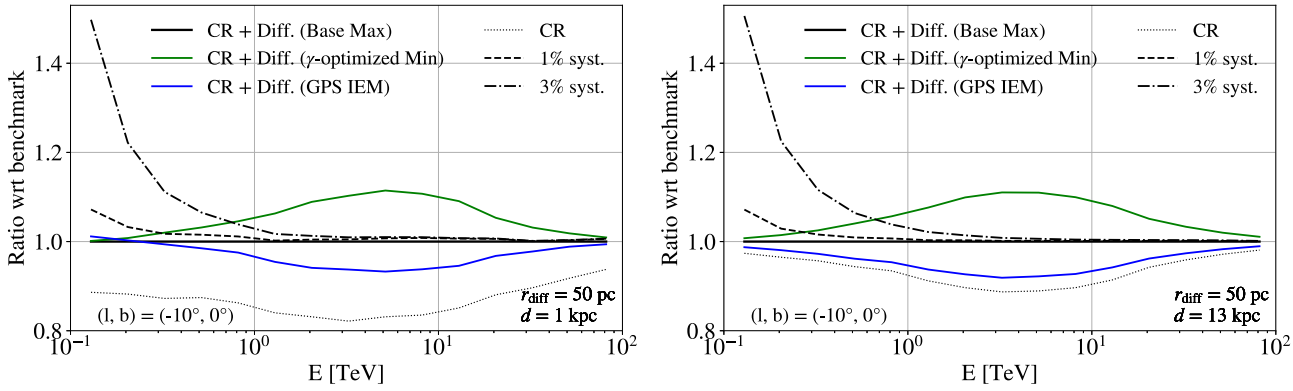

Figure 4. The ratios of the differential energy sensitivity with respect to the benchmark model for a halo at 1 kpc (left-hand panel) and 13 kpc (right-hand panel), considering different IEMs (green and blue line) or no added IE (black thin dotted line). The effect of added systematics on the benchmark model is shown at 1 per cent and 3 per cent levels in black dashed and black dash-dotted lines, respectively.

suppressed diffusion region, whether it be 30, 50, or 80 pc. This is illustrated in Fig. 3 by the set of yellow model curves, and to a lesser extent by the set of red model curves. These plots show that, even for relatively powerful pulsars with injection powers in the 10^{35-36} erg s^{-1} range and located at a few kpc from us, CTA GPS observations are hardly sufficient to discriminate between different extents of the haloes in the core 1–10 TeV range, and definitely too shallow to do so at higher 10–100 TeV energies. At these energies, however, the CTA GPS should enable fine spectral studies of haloes with these properties, reaching above 20–30 TeV for the most powerful and/or closest objects. This will be useful to constrain key parameters of the phenomenon like the injection spectrum or the momentum dependence of suppressed diffusion.

Conversely, there is more potential in the 0.1–1 TeV band to constrain the halo size, because particles radiating in this band have a larger propagation range and fill the halo out to larger distances, to a point that the corresponding emission morphology is sensitive to the location of the suppressed diffusion region boundary. This is illustrated in the right-hand panels of Fig. 3 by the set of purple model curves, to be compared with the predicted angular decomposition displayed as purple dots with error bars. This is complemented by the prospect of fine spectral studies down to or even below 100 GeV, as illustrated in Fig. 2.

When it comes to the study of pulsar haloes, CTA can therefore be expected to nicely complement HAWC and LHAASO by, among other things, offering an extension of the energy coverage below 1 TeV, in a regime where the emitting particles are proportionally less affected by energy losses and can thus probe the entirety of the suppressed diffusion region. The longer lifetime of these particles also implies that the pulsar's proper motion should start to have an impact on the morphology of the halo. This could be an additional advantage as it may provide a specific spectromorphological signature, or a disadvantage as spilling the emission over a larger patch of the sky may reduce the brightness of the signal and increase source confusion. These statements remain qualitatively valid for lower levels of diffusion suppression, such as those possibly involved in Monogem. This would only shift the energy below which the survey is sensitive to the diffusion region extent to higher values, which makes the case even more interesting as discernible effects would be accessible at core energies for CTA where the sensitivity is the highest.

5.2 Accessible fraction of a Galactic population

Based on the analyses presented above of the sensitivity of the survey to representative haloes at various distances, we estimate the fraction of the whole halo population that should be within reach of CTA and, going beyond mere detection, that would allow deeper investigations of the objects.

For each representative halo model (J0633+1746-like or B0656+14-like), and for each distance in the 1–15 kpc range, we performed a series of analyses to compute the following quantities:

(i) Injection power such that the simulated halo signal is detected with a TS of 25 over the full energy range, using the true halo model in the fit process.

(ii) Injection power such that a fit of the simulated halo signal with the true halo model is significantly better than a fit with a simple energy-independent 2D Gaussian intensity distribution.

(iii) Injection power such that a fit of the simulated halo signal with the true halo model is significantly better than a fit with the true model clipped to zero beyond a distance of 30 pc from the pulsar.

(iv) Injection power such that a fit of the simulated halo signal with the true halo model is significantly better than a fit with an alternative halo model having a 50 per cent higher suppressed diffusion coefficient.

In the last three cases, significant means twice the difference in log-likelihood of 16 (which corresponds to a 4σ effect when a variation in only one parameter in nested models is tested, which is not strictly the case in all situations listed above). The 30 pc limit used as criterion in the third test is the typical distance up to which the HAWC observations made it possible to determine a radial intensity profile for J0633+1746 and B0656+14 in Abeysekara et al. (2017). These analyses were done in a simplified framework where observation simulations are based on a source model for the ROI consisting in the halo model and the instrumental background only, while model-fitting to the mock data in the test hypothesis is based on the true models for the halo energy-dependent intensity distribution and instrumental background. In actual data analysis conditions, the source properties are not known a priori, there is source confusion from other unknown astrophysical signals in the field, and instrumental background is not fully under control. So the final results presented below in terms of fraction of the accessible population should be considered as optimistic upper limits.

In Fig. 5, we displayed these requirements in terms of injection power as a function of distance and compare them to the distribution

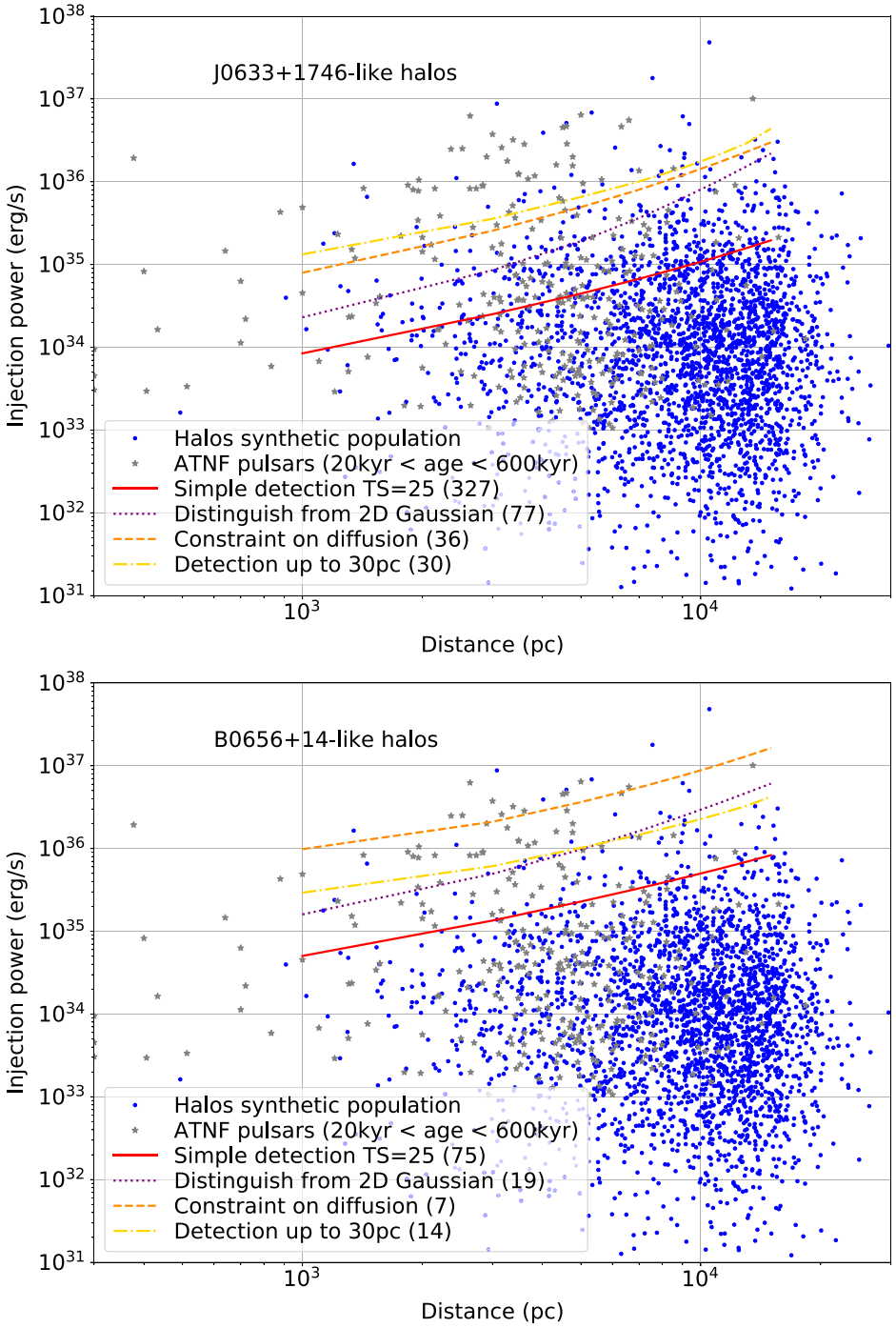

Figure 5. Sensitivity of the survey in terms of particle injection power as a function of distance, for our two representative halo models: with suppressed diffusion typical of J0633+1746 (top) or of B0656+14 (bottom). The blue points marks the locations of mock haloes from our population synthesis. The grey stars mark the locations of pulsars listed in the ATNF data base and having characteristic ages in the 20–600 kyr range. The curves represent sensitivities to various source features: in solid red line, overall detection over the full 0.1–100 TeV range with TS = 25; in purple dotted line, significant separation of the true halo model from a 2D Gaussian intensity distribution; in yellow dot-dashed line, significant detection of emission beyond 30 pc from the pulsar; in orange dashed line, significant separation of the true halo profile from that obtained with a 50 per cent higher diffusion coefficient. For each sensitivity curve, the numbers in parentheses indicate the number of mock haloes lying above the curve.

of mock haloes from the population synthesis presented in Martin et al. (2022b). The number of mock haloes accessible to the survey for a given scientific goal (simple detection, detection of emission up to 30 pc,...) can be evaluated by comparing their actual injection power to that required for a halo at this distance, after correcting for the longitude-dependent sensitivity of the survey. The latter correction is implemented by rescaling our sensitivities, computed for a reference position in the inner Galaxy where the survey sensitivity is at its highest, by the ratio of the targeted survey sensitivity at the halo position to that at our reference position, using the survey

Table 1. List of ATNF pulsars that would yield detectable Geminga-like haloes in the CTA GPS. The last column indicates the kind of constraints that could be obtained: D means plain detection only, M means true energy-dependent halo morphology can be separated from a 2D energy-independent Gaussian, E means extension can be detected beyond 30 pc, and C means the true halo morphology can be separated from one with a 50 per cent higher suppressed diffusion coefficient.

Pulsar	Age (kyr)	Distance (pc)	Spin-down power (erg s^{-1})	Flags
J0002+6216	306.0	6357	1.53×10^{35}	D
B0114+58	275.0	1768	2.21×10^{35}	DMC
J0248+6021	62.4	2000	2.13×10^{35}	DM
B0355+54	564.0	1000	4.54×10^{34}	DM
B0540+23	253.0	1565	4.09×10^{34}	D
J0631+0646	486.0	4583	1.04×10^{35}	D
J0631+1036	43.6	2105	1.73×10^{35}	DM
J0633+0632	59.2	1355	1.19×10^{35}	DM
J0729-1448	35.2	2679	2.81×10^{35}	DM
B0740-28	157.0	2000	1.43×10^{35}	DM
J0834-4159	448.0	5508	9.51×10^{34}	D
J0855-4644	141.0	5638	1.06×10^{36}	DMC
J0901-4624	80.0	3032	4.00×10^{34}	D
J0905-5127	221.0	1330	2.36×10^{34}	D
B0906-49	112.0	1000	4.90×10^{35}	DMEC
J1015-5719	38.6	2732	8.27×10^{35}	DMEC
J1016-5857	21.0	3163	2.58×10^{36}	DMEC
J1019-5749	128.0	10913	1.85×10^{35}	D
J1020-6026	330.0	3277	9.59×10^{34}	D
J1028-5819	90.0	1423	8.32×10^{35}	DMEC
J1044-5737	40.3	1895	8.03×10^{35}	DMEC
B1046-58	20.4	2900	2.00×10^{36}	DMEC
J1052-5954	143.0	3143	1.34×10^{35}	DM
J1055-6028	53.5	3830	1.18×10^{36}	DMEC
J1101-6101	116.0	7000	1.36×10^{36}	DMC
J1105-6107	63.2	2360	2.48×10^{36}	DMEC
J1112-6103	32.7	4500	4.53×10^{36}	DMEC
J1138-6207	149.0	7197	3.03×10^{35}	D
J1151-6108	157.0	2216	3.87×10^{35}	DMC
J1156-5707	172.0	2848	4.37×10^{34}	D
B1259-63	332.0	2632	8.26×10^{35}	DMEC
B1356-60	319.0	5000	1.21×10^{35}	D
J1406-6121	61.7	7297	2.23×10^{35}	D
J1410-6132	24.8	13510	1.01×10^{37}	DMEC
J1412-6145	50.4	7115	1.25×10^{35}	D
J1413-6205	62.8	2150	8.27×10^{35}	DMEC
J1429-5911	60.2	1955	7.75×10^{35}	DMEC
J1437-5959	114.0	8543	1.44×10^{36}	DMEC
J1459-6053	64.7	1840	9.09×10^{35}	DMEC
J1509-5850	154.0	3372	5.15×10^{35}	DMEC
B1508-57	298.0	6835	1.27×10^{35}	D
J1524-5625	31.8	3378	3.21×10^{36}	DMEC
J1531-5610	96.7	2841	9.12×10^{35}	DMEC
J1538-5551	517.0	5985	1.10×10^{35}	D
J1541-5535	62.5	5161	1.14×10^{35}	D
J1548-5607	252.0	5702	8.48×10^{34}	D
J1549-4848	324.0	1308	2.32×10^{34}	D
J1551-5310	36.9	5878	8.25×10^{34}	D
J1601-5335	73.3	3576	1.03×10^{35}	D
B1607-52	559.0	2949	3.36×10^{34}	D
J1632-4757	240.0	4836	4.98×10^{34}	D
J1636-4440	70.1	12455	2.09×10^{35}	D
B1634-45	590.0	3442	7.52×10^{34}	D
J1637-4642	41.2	4410	6.40×10^{35}	DMEC
J1638-4608	85.6	4570	9.44×10^{34}	D
J1643-4505	118.0	4738	9.39×10^{34}	D
B1643-43	32.5	6226	3.58×10^{35}	DM
J1648-4611	110.0	4468	2.09×10^{35}	DM
J1702-4128	55.1	3971	3.42×10^{35}	DM
J1705-3950	83.4	3426	7.37×10^{34}	D
J1715-3903	118.0	3737	6.84×10^{34}	D

Table 1 *– continued*

Pulsar	Age (kyr)	Distance (pc)	Spin-down power (erg s^{-1})	Flags
J1718-3825	89.5	3488	1.25×10^{36}	DMEC
B1718-35	176.0	4600	4.51×10^{34}	D
B1719-37	344.0	2477	3.26×10^{34}	D
J1723-3659	400.0	3497	3.80×10^{34}	D
B1727-33	26.0	3488	1.23×10^{36}	DMEC
J1737-3137	51.4	4162	5.99×10^{34}	D
J1738-2955	85.7	3460	3.71×10^{34}	D
J1739-3023	159.0	3074	3.01×10^{35}	DMC
J1740+1000	114.0	1227	2.32×10^{35}	DMEC
J1747-2958	25.5	2520	2.51×10^{36}	DMEC
B1754-24	285.0	3124	4.00×10^{34}	D
B1758-23	58.3	4000	6.20×10^{34}	D
J1809-1917	51.4	3268	1.78×10^{36}	DMEC
J1811-1925	23.3	5000	6.42×10^{36}	DMEC
J1813-1246	43.4	2635	6.24×10^{36}	DMEC
J1815-1738	40.4	4887	3.93×10^{35}	DM
B1822-14	195.0	4440	4.11×10^{34}	D
B1823-13	21.4	3606	2.84×10^{36}	DMEC
J1828-1057	189.0	3648	5.47×10^{34}	D
J1828-1101	77.2	4767	1.56×10^{36}	DMEC
B1828-11	107.0	3147	3.56×10^{34}	D
J1831-0952	128.0	3683	1.08×10^{36}	DMEC
B1830-08	147.0	4500	5.84×10^{35}	DMEC
B1832-06	120.0	5041	5.58×10^{34}	D
J1835-0944	525.0	4215	5.64×10^{34}	D
J1835-1106	128.0	3159	1.78×10^{35}	DM
J1837-0604	33.8	4771	2.00×10^{36}	DMEC
J1838-0453	51.9	6629	8.31×10^{34}	D
J1838-0549	112.0	4061	1.01×10^{35}	D
J1838-0655	22.7	6600	5.55×10^{36}	DMEC
J1841-0345	55.9	3776	2.69×10^{35}	DM
B1838-04	461.0	4399	3.91×10^{34}	D
J1841-0524	30.2	4125	1.04×10^{35}	D
J1846+0919	360.0	1530	3.41×10^{34}	D
J1850-0026	67.5	6710	3.34×10^{35}	D
J1853-0004	288.0	5339	2.11×10^{35}	D
J1853+0056	204.0	3841	4.03×10^{34}	D
B1853+01	20.3	3300	4.30×10^{35}	DMEC
J1856+0245	20.6	6318	4.63×10^{36}	DMEC
J1857+0143	71.0	4566	4.51×10^{35}	DMC
J1906+0746	113.0	7400	2.68×10^{35}	D
J1907+0918	38.0	8224	3.22×10^{35}	D
J1909+0749	24.7	8286	4.50×10^{35}	D
J1909+0912	98.7	7608	1.28×10^{35}	D
J1913+0904	147.0	2997	1.60×10^{35}	DM
J1913+1011	169.0	4613	2.87×10^{36}	DMEC
J1916+1225	154.0	6486	7.87×10^{34}	D
J1925+1720	115.0	5060	9.54×10^{35}	DMEC
J1928+1746	82.6	4337	1.60×10^{36}	DMEC
B1930+22	39.8	10900	7.54×10^{35}	D
J1934+2352	21.6	12204	9.08×10^{35}	D
J1935+2025	20.9	4598	4.66×10^{36}	DMEC
J1938+2213	62.0	3419	3.66×10^{35}	DMC
B1951+32	107.0	3000	3.74×10^{36}	DMEC
J1954+2836	69.4	1960	1.05×10^{36}	DMEC
J1958+2846	21.7	1950	3.42×10^{35}	DMC
J2006+3102	104.0	6035	2.24×10^{35}	D
J2021+4026	76.9	2150	1.16×10^{35}	DM
J2032+4127	201.0	1330	1.52×10^{35}	DM
J2238+5903	26.6	2830	8.89×10^{35}	DMEC
J2240+5832	144.0	7275	2.21×10^{35}	D

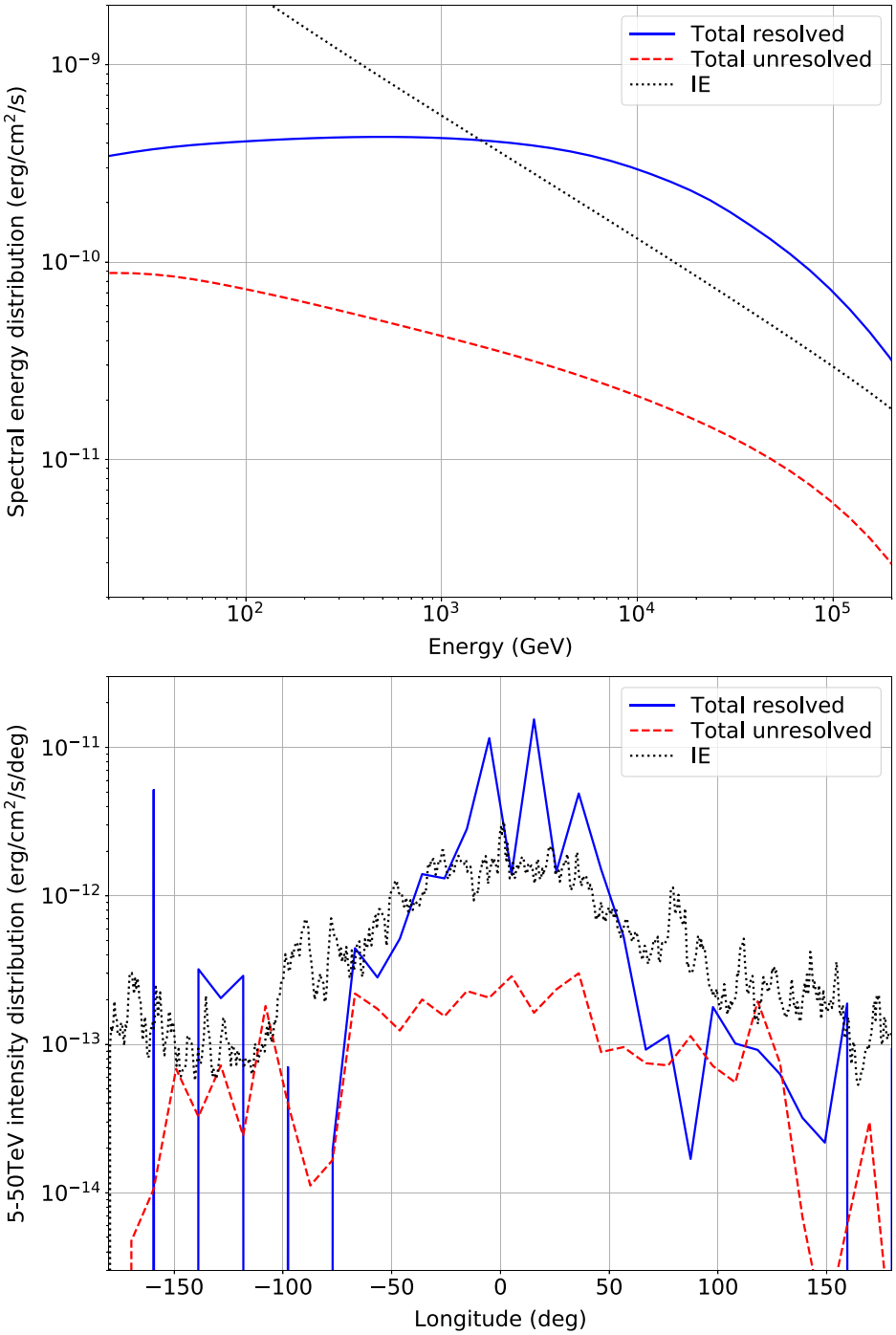

Figure 6. Spectrum and longitude distribution of the total emission from resolved or unresolved haloes, when the representative halo model features suppressed diffusion typical of J0633+1746. Both are integrated over the survey footprint. For comparison, the total emission from interstellar radiation is also displayed, using the 'Base Max' model setup from De la Torre Luque et al. (2022). The longitude distributions for halo emission are computed over 10-degree bins to smooth out the fluctuations from the actual realization of the population synthesis.

performance description in Cherenkov Telescope Array Consortium (2019).

For objects at a distance in the 1–15 kpc range, about 350 (respectively 100) haloes would be detectable if they are assumed to be J0633+1746-like (respectively B0656+14-like). The plot however illustrates that a much lower number of objects are expected to allow deeper investigation of their physical properties. Only 30 (respectively 14) J0633+1746-like (respectively B0656+14-like) haloes can be significantly detected up to 30 pc, which should make it possible to perform meaningful angular decomposition of their emission, as illustrated in Fig. 3. Similarly, significant constraint on the suppressed diffusion coefficient can be achieved for only 40 haloes in the J0633+1746-like model setup, and four times fewer objects with the B0656+14-like one.

The prospects for mere detection of J0633+1746-like pulsar haloes are about twice those obtained in Martin et al. (2022b) from

a simple flux criterion (about 160 objects, see their table 2). This is not surprising as the present estimates are based on a method that exploits the full spectromorphological signature of haloes over a broad energy range. The number of detectable J0633+1746-like pulsar haloes thus becomes comparable to the number of detectable PWNe presented in Remy et al. (2022).

5.3 Promising pulsar candidates

In the plots of Fig. 5, we displayed the positions of known pulsars from the Australia Telescope National Facility (ATNF) data base with characteristic ages in the 20–600 kyr range (younger pulsars are expected to be in their PWN stage, and older ones to be too faint for detection). Our predicted sensitivity limits can be used to select those ATNF pulsars that could be detectable if they were to develop a halo, under the assumption that 100 per cent of their spin-down power is injected into non-thermal particles.

We present in Table 1 a list of those 122 pulsars that should be detectable according to our sensitivity estimate, and under the assumption that they develop a Geminga-like halo. We specify for each of them whether they should allow deeper investigations beyond simple detection. Out of 122, 65 can be distinguished from a 2D energy-independent Gaussian intensity distribution and 41 can be detected up to 30 pc at least. These numbers are comparable to those obtained from the population synthesis. Not all pulsars listed in this table are expected to be good halo candidates, in particular because some may still be in their PWN stage and have unambiguously been identified as such already, or have actual injection efficiencies lower than 100 per cent, but the sample is a good starting point for a selection of targets.

5.4 Diffuse emission from the unresolved population

Fig. 6 shows the properties of the diffuse emission contributed to by the ∼2000 or more pulsar haloes that are not detectable individually, for one single realization of the population synthesis and when the representative halo model features suppressed diffusion typical of J0633+1746.

Integrated over the whole survey footprint, this emission is subdominant compared to that from interstellar radiation, described with the 'Base Max' model from De la Torre Luque et al. (2022), with a maximum contribution at the level of 10–20 per cent in the 10–100 TeV range. Yet, the longitude distribution shows a more contrasted picture, with regions of comparable 5–50 TeV intensity such as the Cygnus-Cassiopeia portion of the plane, while interstellar emission in the inner Galaxy is almost an order of magnitude above that from unresolved haloes.

When haloes are modelled with shallower suppressed diffusion typical of B0656+14, they are on average fainter and more extended, hence less likely to be detected (four times fewer objects are detectable in the survey; see Section 5.2). Both effects combine to eventually yield an emission from unresolved haloes that is more intense than when haloes are modelled with suppressed diffusion typical of J0633+1746, and comparable to interstellar emission along the plane.

Last, we emphasize that the above statements hold under the strong assumption that all middle aged pulsars develop haloes. If only a small fraction (5–10 per cent of them) do so, as suggested in Martin et al. (2022a), haloes become negligible in terms of contribution to the Galactic diffuse emission.

6 CONCLUSIONS

We presented a quantitative assessment of the prospects for the detection and study of the emerging class of pulsar haloes in the observations planned for the CTA GPS. Using a simple phenomenological two-zone diffusion model for individual pulsar haloes and their population in the Milky Way, we simulate a realistic study of these objects in the framework of a full spatial-spectral likelihood analysis of simulated survey observations.

For a halo model setup consistent with the HAWC observations of the halo around PSR J0633+1746, and under the assumption that all middle-aged pulsars that exited their original nebula develop a halo, we show that about three hundreds objects could give rise to detectable emission components in the survey. Yet, only a third of them could be identified through their energy-dependent morphology, and only one tenth of them would allow the derivation of strong constraints on key physical parameters like the magnitude or extent of suppressed diffusion around the pulsar. These numbers are roughly divided by four when using a model setup consistent with the HAWC observations of PSR B0656+14 instead.

For pulsar haloes sustained by particle injection power in the range 10^{35-36} erg s^{-1} and located out to a few kpc from us, the CTA GPS observations should enable fine spectral studies from hundreds of GeV or below up to a few tens of TeV. The 0.1–1 TeV band accessible to CTA holds a lot of potential for constraining the transport properties in haloes. CTA can be expected to complement HAWC and LHAASO by extending the energy coverage below 1 TeV , in a regime where the emitting particles are proportionally less affected by energy losses and can thus probe a larger volume around the pulsar.

Last, we provide a list of known pulsars that could be hosting a detectable (Geminga-like) halo in the GPS, together with information about the likelihood to achieve different analysis goals if it is the case (from simple detection to the derivation of meaningful constraint of the suppressed diffusion characteristics).

ACKNOWLEDGEMENTS

We warmly thank Rubén López-Coto and Daniela Hadasch for carefully reading our manuscript and helpful comments. The work of CE is supported by the 'Agence Nationale de la Recherche' through grant ANR-19-CE31-0005-01 (PI: F. Calore). The work of CE has been supported by the EOSC Future project which is co-funded by the European Union Horizon Programme call INFRAEOSC-03-2020, Grant Agreement 101017536. The work of PM is supported by the 'Agence Nationale de la Recherche' through grant ANR-19-CE31-0014 (GAMALO project, PI: P. Martin).

Software: ASTROPY (The Astropy Collaboration 2013, 2018, 2022), CTOOLS (v1.6.2) (Knödlseder et al. 2016), GAMMAPY (v1.0) (Deil et al. 2017; Acero et al. 2022),HEALPY (Górski et al. 2005; Zonca et al. 2019), IMINUIT (Dembinski, Ongmongkolkul et al. 2020), JUPYTER (Kluyver et al. 2016), MATPLOTLIB (Hunter 2007), NUMPY (Harris et al. 2020), SCIPY (Virtanen et al. 2020).

DATA AVAILABILITY

The data that support the findings of this study are available from the corresponding authors [CE, VV, PM] upon reasonable request.

REFERENCES

Abdalla H. et al., 2018a, A&A, 612, A1
Abdalla H. et al., 2018b, A&A, 612, A2
Abdalla H. et al., 2019, A&A, 621, A116
Abdalla H. et al., 2021, ApJ, 917, 6
Abeysekara A. U. et al., 2017, Science, 358, 911
Abramowski A., et al., 2014, Phys. Rev. D, 90, 122007
Acero F. et al., 2022, Gammapy: Python toolbox for gamma-ray astronomy. Available at: https://doi.org/10.5281/zenodo.7311399
Acharyya A., et al., 2021, J. Cosmol. Astropart. Phys., 2021, 057
Ackermann M., et al., 2012, ApJ, 750, 3
Aharonian F. et al., 2021, Phys. Rev. Lett., 126, 241103
Albert A. et al., 2020, ApJ, 905, 76
Amato E., 2020, PoS, HEPROVII, 033
Bartels R., Gaggero D., Weniger C., 2017, J. Cosmol. Astropart. Phys., 05, 001
Bucciantini N., Olmi B., Del Zanna L., 2020, J. Phys. Conf. Ser., 1623, 012002
Bykov A. M., Amato E., Petrov A. E., Krassilchtchikov A. M., Levenfish K. P., 2017, Space Sci. Rev., 207, 235
Cherenkov Telescope Array Consortium 2019, Science with the Cherenkov Telescope Array. World Scientific, Singapore
Cherenkov Telescope Array Observatory and Cherenkov Telescope Array Consortium, 2021, CTAO Instrument Response Functions-prod5 version v0.1. Available at: https://doi.org/10.5281/zenodo.5499840
Cowan G., Cranmer K., Gross E., Vitells O., 2011, Eur. Phys. J. C, 71, 1554
De la Torre Luque P., Gaggero D., Grasso D., Fornieri O., Egberts K., Steppa C., Evoli C., 2022, preprint (arXiv:2203.15759)
Deil C. et al., 2017, in Proc. 35th Int. Cosmic Ray Conf. (ICRC2017), Gammapy - A prototype for the CTA science tools. ICRC, Busan, p. 766
Dembinski H., Ongmongkolkul P., et al., 2020, scikit-hep/iminuit. Available at: https://doi.org/10.5281/zenodo.3949207
de Oña Wilhelmi E., López-Coto R., Amato E., Aharonian F., 2022, ApJ, 930, L2
Di Mauro M., Manconi S., Donato F., 2019, Phys. Rev. D, 100, 123015
Di Mauro M., Manconi S., Donato F., 2020, Phys. Rev. D, 101, 103035
Dundovic A., Evoli C., Gaggero D., Grasso D., 2021, A&A, 653, A18
Evoli C., Linden T., Morlino G., 2018, Phys. Rev. D, 98, 063017
Evoli C., Amato E., Blasi P., Aloisio R., 2021, Phys. Rev. D, 103, 083010
Fang K., Bi X.-J., Yin P.-F., 2019, MNRAS, 488, 4074
Fermi-LAT collaboration, 2022, Public list of LAT-Detected gamma-ray pulsars. Available at: https://confluence.slac.stanford.edu/display/GLAMCOG/Public+List+of+LAT-Detected+Gamma-Ray + Pulsars
Gaensler B. M., Slane P. O., 2006, ARA&A, 44, 17
Górski K. M., Hivon E., Banday A. J., Wand elt B. D., Hansen F. K., Reinecke M., Bartelmann M., 2005, ApJ, 622, 759
Harris C. R. et al., 2020, Nature, 585, 357
Hunter J. D., 2007, Comput. Sci. Eng., 9, 90
Kluyver T. et al., 2016, in Loizides F., Scmidt B.eds, Positioning and Power in Academic Publishing: Players, Agents and Agendas. IOS Press, Amsterdam, p. 87. Available at: https://eprints.soton.ac.uk/403913/
Knödlseder J. et al., 2016, A&A, 593, A1
Linden T., Auchettl K., Bramante J., Cholis I., Fang K., Hooper D., Karwal T., Li S. W., 2017, Phys. Rev. D, 96, 103016
López-Coto R., Giacinti G., 2018, MNRAS, 479, 4526
López-Coto R., Wilhelmi E. d. O., Aharonian F., Amato E., Hinton J., 2022, Nat. Astron., 6, 199
Martin P., Marcowith A., Tibaldo L., 2022a, A&A, 665, A132
Martin P., Tibaldo L., Marcowith A., Abdollahi S., 2022b, A&A, 666, A7
Mukhopadhyay P., Linden T., 2022, Phys. Rev. D, 105, 123008
Pétri J., 2016, J. Plasma Phys., 82, 635820502
Pétri J., 2018, MNRAS, 477, 1035
Principe G., Mitchell A. M. W., Caroff S., Hinton J. A., Parsons R. D., Funk S., 2020, A&A, 640, A76
Remy Q., Tibaldo L., Acero F., Fiori M., Knödlseder J., Olmi B., Sharma P., 2022, in Proc. 37th Int. Cosmic Ray Conf. (12-23 July 2021), Vol. 395, Survey of the Galactic Plane with the Cherenkov Telescope Array. ICRC, Berlin, p. 886
Scott Wakely and Deirdre Horan, 2022, TeVCat. Available at: http://tevcat2.uchicago.edu/
Silverwood H., Weniger C., Scott P., Bertone G., 2015, J. Cosmol. Astropart. Phys., 03, 055
Tang X., Piran T., 2019, MNRAS, 484, 3491
The Astropy Collaboration 2013, A&A, 558, A33
The Astropy Collaboration 2018, AJ, 156, 123
The Astropy Collaboration 2022, ApJ, 935, 167
Thompson D. J., 2008, Rep. Progr. Phys., 71, 116901
Virtanen P. et al., 2020, Nat. Methods, 17, 261
Xi S.-Q., Liu R.-Y., Huang Z.-Q., Fang K., Wang X.-Y., 2019, ApJ, 878, 104
Zhang Y., Liu R.-Y., Chen S. Z., Wang X.-Y., 2021, ApJ, 922, 2, 130
Zonca A., Singer L., Lenz D., Reinecke M., Rosset C., Hivon E., Gorski K., 2019, J. Open Source Softw., 4, 1298

APPENDIX A: COMPARISON BETWEEN CTOOLS AND GAMMAPY

In this appendix, we comment on the differences that occur between a gamma-ray analysis conducted with `ctools` and `gammapy` (Deil et al. 2017). Both software packages are publicly available and designed to perform scientific analyses on very high-energy gamma-ray data. While all results shown in the main text of this work have been derived with the functionalities of `ctools`, we repeated a small part of the analysis steps with templates generated by `gammapy` since it exhibits the same appeal as `ctools` and offers the opportunity to analyse data sets from other instruments than CTA.

To this end, we (re-)examine the 5σ detection sensitivity to a Geminga-like pulsar halo with a diffusion zone size of $r_{\rm diff} = 30$ pc located at various distances from the Solar system (cf. Fig. 2, right-hand panel). The resulting sensitivity values are displayed in Fig. A1, where the solid lines represent the values obtained with `gammapy` while the dotted lines are the corresponding ctools equivalents. Up to energies of $\sim$1 TeV, both software packages agree reasonably well with each other. At higher energies, the results start to diverge in a way that the templates prepared with ctools lead to systematically better sensitivities. This effect may be as pronounced as $\sim$ 20 per cent for the last energy bin and a halo at 1 kpc distance. None the less, the profiles of the sensitivity curves are fairly similar. The existing differences might be explained with the explicit approach implemented in each software package to derive the Asimov prediction for a given flux model, which – to the best of our knowledge – is indeed different.

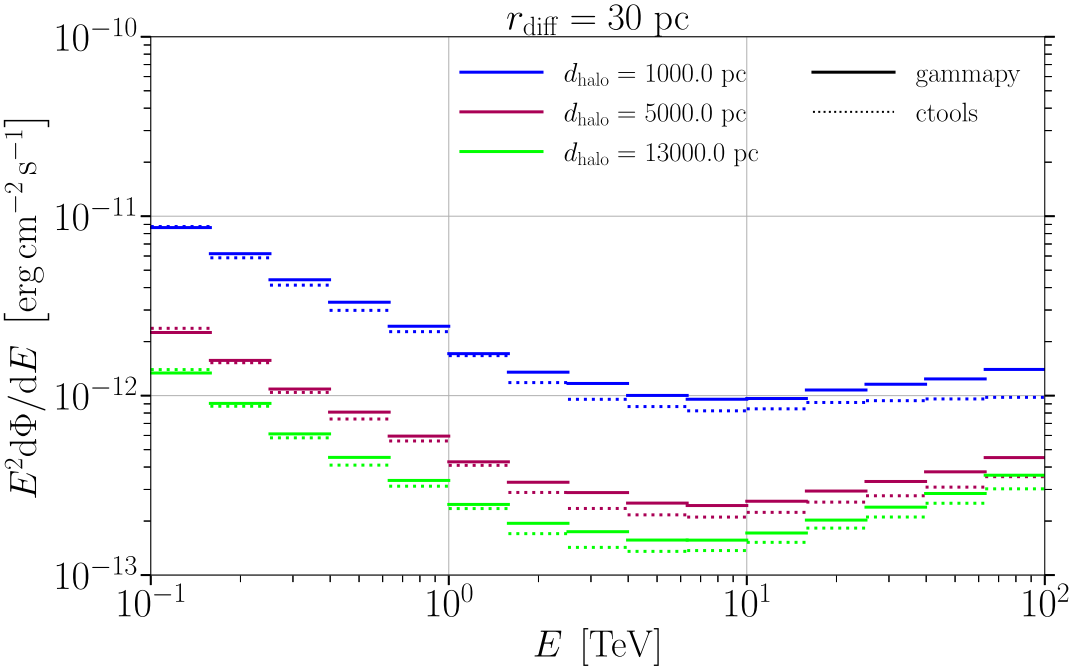

Figure A1. Differential spectral detection sensitivity (5σ) to Geminga-like pulsar haloes exhibiting a diffusion zone size of 30 pc located at $(\ell, b) = (-10^\circ, 0^\circ)$ at various distances from the Earth studied under the conditions of CTA's Galactic plane survey. The solid sensitivity values represent the results obtained by using `gammapy` routines for the convolution with CTA's IRFs while the dotted values represent the equivalent scenario for templates generated with ctools.

APPENDIX B: THE FULL GPS EXPOSURE MAPS

In addition to Fig. 1 which shows the exposure of the planned GPS observations overlaid with synthetic TeV halo population over a limited longitude range, we show in Fig. B1 the exposure of the full GPS. The top (bottom) panels show all (only detected) TeV haloes within our synthetic population. The spherical shape of the TeV halo markers is preserved, with their size scaled in accordance with the latitude axis. The majority of the sources are in the central region which is expected to receive the most observation time and reach the deepest exposure.

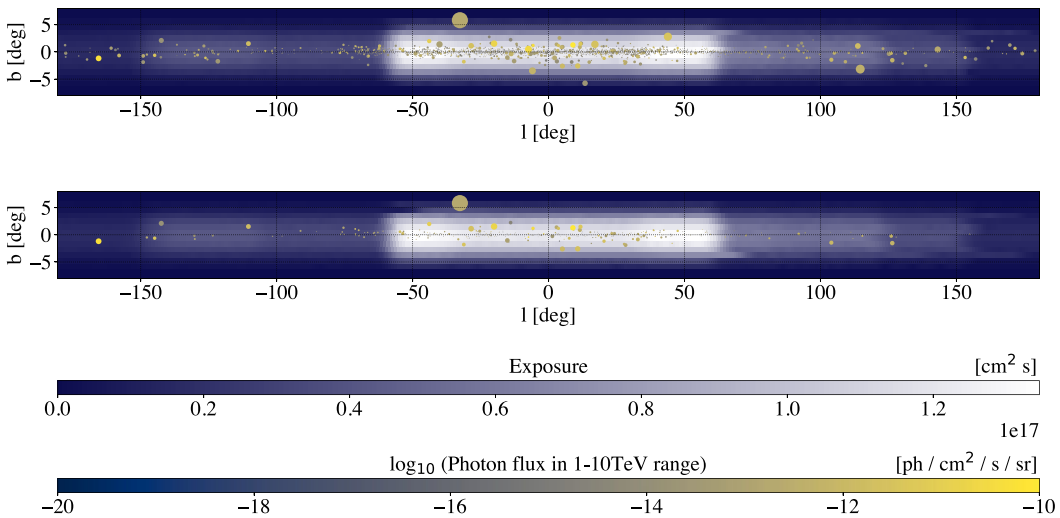

Figure B1. The exposure for the planned GPS observations overlaid with synthetic TeV halo population, showing the full Galactic plane. Note that, in order to preserve spherical shape of sources, they are plotted assuming the pixel size in the b direction. The most sources from our synthetic halo population are in the region that has the deepest exposure. Top: All simulated sources. Bottom: Only resolved sources (see Section 5.2).

APPENDIX C: IMPACT FROM IE MODEL

In a realistic analysis, the true IE properties are not known. In this appendix, we explore how using in model fitting a diffuse emission model other than the true one used in data simulation can affect the derived differential sensitivity. In a realistic data analysis, multiple IE models may be tested and fitted to the data, and the model yielding the best fit is selected for further analysis. We simulated mock data using different diffuse emission models and explored the log-likelihood variations from assuming different diffuse emission models. The resulting values are shown in Table C1. The best fit is naturally obtained when using in model fitting the same IE model that was used for producing the mock data, and we retain the corresponding results as a measure of the impact of the true IE properties. The second best fit for each data set is highlighted in grey, and we retain the corresponding results as a measure of the impact of using an imperfect IE model on sensitivity. The comparison of the differential sensitivities with respect to our benchmark model (using Base Max IEM) for the best fit and second best-fitting IE combinations is shown in Fig. C1. The impact of the different variants for IE modelling is very modest, while the worsening of sensitivity can reach up to a factor of 4 at the highest energies when using an inadequate model.

Table C1. Table of the log-likelihood value difference between a fit with the same IE as used to prepare the mock data and alternative IEMs, considering a source at 1 kpc (top) and 13 kpc (bottom) distance from the Sun. The second best-fitting models for each mock data are highlighted in grey and the differential sensitivity with respect to the benchmark for these IE combinations is shown in Fig. C1.

		Source at 1 kpc distance		
Model | Data	Base max	γ-Optimized min	γ-Optimized max	Base min
Base max	0	502773	305625	45001
γ-opt. min	483948	0	95809	366297
γ-opt. min	299580	97392	0	193519
Base min	44422	376630	193474	0
		Source at 13 kpc distance		
Model | Data	Base max	γ-Optimized min	γ-Optimized max	Base min
Base max	0	64243	38223	4763
γ-opt. min	62116	0	10681	46699
γ-opt. max	38079	10801	0	23917
Base min	4824	47255	23157	0

This paper has been typeset from a TEX/LATEX file prepared by the author.